ANDRA BGR CRIEPI ENRESA GRS HSK IRSN JAEA NAGRA OBAYASHI SCK•CEN SWISSTOPO
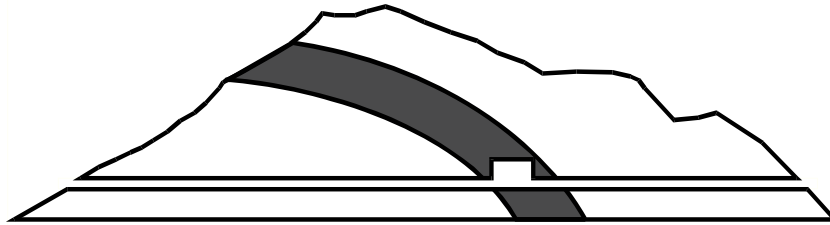
Mont Terri Project

TECHNICAL REPORT 2007-05
(TN 2007-45)

November 2007

LT Experiment:
Strength and Deformation of Opalinus Clay

W. Gräsle and I. Plischke

Federal Institute for Geosciences and Natural Resources (BGR), Germany

Distribution:

Standard distribution:

ANDRA (J. Delay)

BGR (H. J. Alheid)

CRIEPI (K. Kiho)

ENRESA (J. Astudillo)

GRS (T. Rothfuchs)

HSK (E. Frank)

IRSN (J.-M. Matray)

JAEA (N. Shigeta)

Nagra (M. Hugi)

Obayashi (H. Kawamura, T. Tanaka)

SCK•CEN (G. Volckaert)

SWISSTOPO (P. Bossart and P. Hayoz)

GI AG (Ch. Nussbaum)

Additional distribution:

Every organisation & contractor takes care of their own distribution.

TABLE OF CONTENTS

ABSTRACT

Long-term multistep creep tests on samples from Mont Terri BLT-14 and BLT-15 boreholes were carried out. The tests were performed at 30°C under drained conditions. Sample orientations parallel (BLT-14) as well as perpendicular (BLT-15) to the bedding plane were investigated to account for the anisotropy of the material.

A new type of triaxial test using a complex process path was developed to yield as much information on the mechanical behavior as possible from a single sample. Relatively large data sets not affected by the variations between different samples are considered to facilitate the derivation of a constitutive equation for Opalinus clay. A first test of the new experimental layout was carried out on a BHE-B1 sample, investigating the limit of linear elastic behavior, the shear failure limit, and the residual strength as functions of minimum principal stress. The test was performed under undrained conditions to allow for the investigation of possible pore pressure effects.

1 CONTEXT AND AIM OF THE STUDY

The long-term safety of mines and repositories for radioactive or toxic wastes can be predicted if the mechanical behavior and hydraulic properties of the host rock can be described reliably. For this purpose laboratory tests were performed to investigate the deformation of the host rock at all relevant stress and temperature conditions.

At the Mont Terri test site in Switzerland the Opalinus clay stone is investigated for its suitability for the disposal of radioactive waste. The LT-experiment (Laboratory Testing) is focused on the investigation of mechanic and hydraulic material properties and behavior (in particular creep, dilatation, healing, strength, permeability and anisotropy) in a relevant range of stress states and temperatures. The tests are performed in the laboratories of BGR.

Like all bedded rocks, Opalinus clay has different mechanical properties in and perpendicular to its foliation plane i.e. orthorhombic symmetry with three mutually perpendicular planes of symmetry. BGR's laboratory program will describe and define all the rock mechanic properties of the Opalinus clay parallel as well as orthogonal to the bedding plane (two-dimensional orthotropic solid). We intend especially to investigate the deformation processes, the distortion-dilatation relation, and to obtain a constitutive equation for the Opalinus clay from the Mont Terri site.

2 SAMPLING AND PREPARATION

Several drilling campaigns were accomplished by BGR during phase 11+12 to obtain rock samples for the ongoing and planned tests. The boreholes BLT-14 to BLT-18 are located close to the Northern end of Gallery 98 in the shaly facies of the Opalinus clay at the Mont Terri site (Fig. 1). The starting points of the boreholes are in a distance of 8 to 10 m from the boundary between Opalinus clay and Jurensis marls.
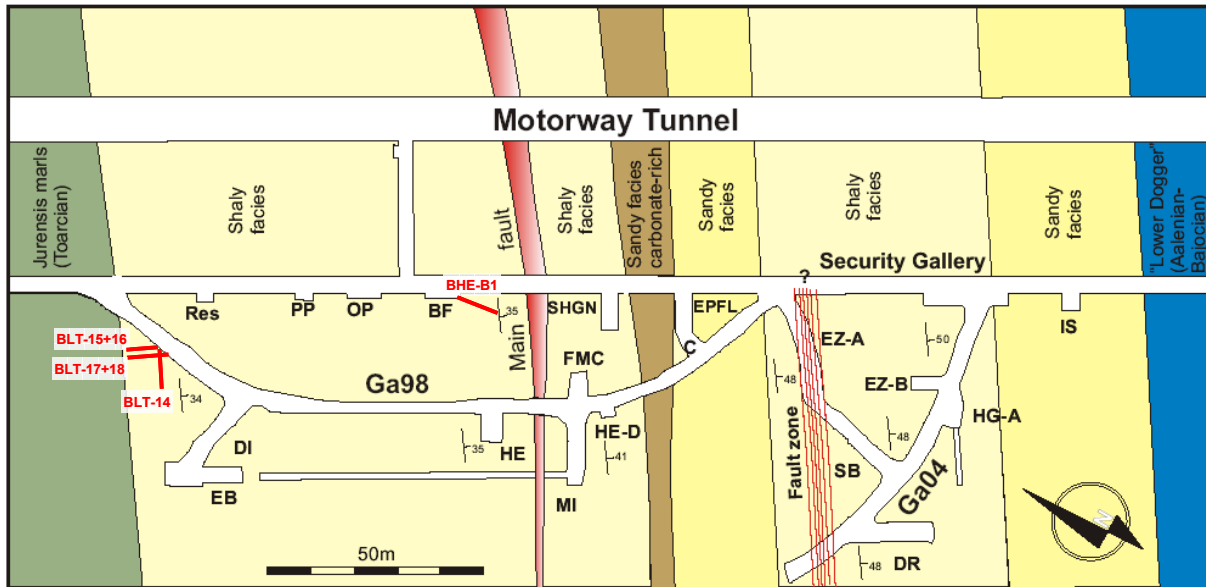
Fig. 1 Location of the BLT-14 to BLT-18 boreholes drilled during phase 11+12, and of the BHE-B1 borehole used in the complex strength test.

In January 2007 borehole BLT-14 was drilled parallel to the bedding within strike. End of March 2007 BLT-15 was drilled perpendicular to the bedding, followed by BLT-16 parallel to the bedding within fall. BLT-15 went into Jurensis marls at a depth of approximately 8.2 m.

Finally, BLT-17 and BLT-18 were drilled in July 2007. BLT-17 which has an angle of 60° towards the bedding normal to strike and is almost parallel to the security gallery was abandoned because all cores broke apart. The vertical, axially aligned interfaces were obviously freshly formed fractures (Fig. 2). Considering that BLT-17 is located in the zone of increased stresses slightly outside the EDZ of the security gallery, these fractures may most likely result from the quick unloading of the material during the drilling process. Thus, the attempt to gain cores in this alignment was not repeated at this location. Instead, BLT-18 was drilled 30° towards the bedding normal to strike.

Opalinus clay material is very susceptible to damage by desiccation (SCHNIER, 2004). Furthermore, the impact of oxygen significantly affects the material properties. This is mainly attributed to the oxidation of pyrite and the subsequent formation of gypsum.

To minimize these perturbations, the samples were sealed in air-tight aluminum coated foils as quick as possible. Transport and storage of the sealed samples is done in special liners (Fig. 3), filled with nitrogen as a protective gas at a pressure of 3 bar. This will keep the protected conditions even in case of a perforation of the sealing foil.

Fig. 2 Core from BLT-17 showing freshly formed axial fractures. There is neither a slickenside (which would indicate a tectonic fault) nor any trace of gypsum crystals (which generate within a few days in any crack opened in the EDZ due to the impact of atmospheric oxygen) on the interface.

Fig. 3   The liners used for transport and storage of core samples.

Sample preparation was carried out immediately before the tests. They were cut to length with a band saw, and then they were trimmed to smooth cylindrical shape on a lathe. To avoid undesirable friction effects during the tests the samples were covered with a Teflon foil before they were coated in rubber tubes which prevent any contact between the samples and the oil pressurizing the Karman cell.

3   GEOLOGICAL AND MINERALOGICAL DESCRIPTION

The general mineralogical properties of the host rocks at the Mont Terri laboratory have been summarized by THURY & BOSSART (1999). Shaly, calcareous-sandy and sandy facies are distinguished. Their main difference in terms of mineralogical composition is the content of clay minerals and quartz. The content of feldspars is similar (see also PEARSON ET AL. 2003). All samples used for the rock mechanical experiments covered by this report belong to the shaly facies.

Detailed investigations of the mineralogical composition of the rocks from BLT-14 and BLT-15 are in work. First results show that the carbonate contents of the sample from BLT-14/05 is 19.2 wt-% and of BLT-14/11 15.5 wt.-%. At BLT-14/05 the carbonate is located as calcite crystals in zones, whereas at BLT-14/11 carbonate exists as detritus in small layers. More microstructural investigations of Opalinus clay from Mont Terri especially of the distribution of carbonate are shown at KLINKENBERG ET AL. (2007). Pictures of all tested samples are in Fig. 5 and Fig. 6.

4 DRAINED CREEP TEST

4.1 CONCEPT AND OBJECTIVE

The long term behavior of rock material under the impact of anisotropic stresses is a key parameter for the evolution of any underground excavation (convergence, reduction of deviatoric stress). Therefore, creep tests where carried out on Mont Terri Opalinus clay. The anisotropy of the clay has to be considered in these tests. As the pore pressure is expected to influence the creep behavior of Opalinus clay a well defined hydraulic regime has to be kept during the tests.

The creep tests were carried out in conventional Karman cells. Four samples measuring approx. 100 mm in diameter and 220 mm in length were investigated. Two samples from BLT-14 were drilled parallel to the bedding plane (p-samples); the others from BLT-15 were drilled normal to bedding (s-samples, Fig. 4). Fig. 5 and Fig. 6 display the prepared samples before the tests. A summary of the tested samples and the test procedure is given in Tab. 1.
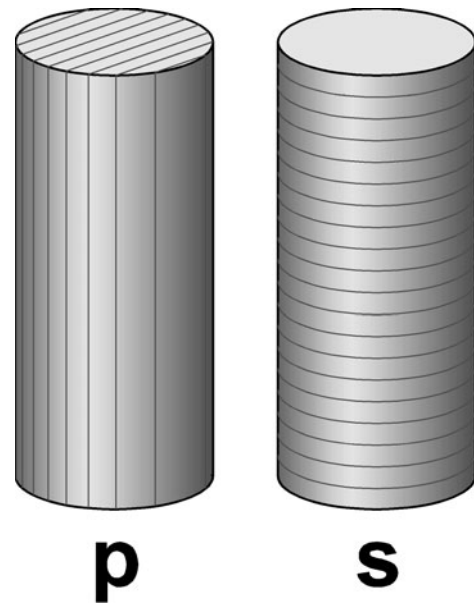
Fig. 4 The alignment of cylindrical samples with respect to the bedding for p- and s-geometry.

Tab. 1 Sample characterization and test layout for the drained creep tests.

sample		BLT-14/05	BLT-14/11	BLT-15/4	BLT-15/8
file-number [1]		07001	07002	07004	07005
diameter [mm]		99.9	99.9	99.8	99.9
length [mm]		220.0	220.0	218.2	220.7
bulk density [g/cm3]		2.448	2.439	2.444	2.447
mass [kg]		4.222	4.207	4.171	4.232
velocity p-wave [m/s]		3320	3325	N.T.[2]	2698
velocity s-wave [m/s]		N.T.[2]	N.T.[2]	N.T.[2]	N.T.[2]
orientation to bedding		p	p	s	s
depth [m]		3.00 – 3.22	9.74 – 9.96	4.53 – 4.75	7.37 – 7.60
cell pressure σ_x [MPa]		10	10	10	10
duration of phases [d]	$\sigma_z - \sigma_x =$ 0.5 MPa	2	2	1	1
	$\sigma_z - \sigma_x =$ 1 MPa	17	17	17	17
	$\sigma_z - \sigma_x =$ 5 MPa	36	36	38	38
	$\sigma_z - \sigma_x =$ 8 MPa	50	50	–	–
	$\sigma_z - \sigma_x =$ 10 MPa	79	79	52	52
	$\sigma_z - \sigma_x =$ 13 MPa	69	69	69	69

[1] The file-number identifies a sample in the BGR laboratory documentation system LIMS.
[2] N.T. = no transmission of signal.

Ø 100 × 220
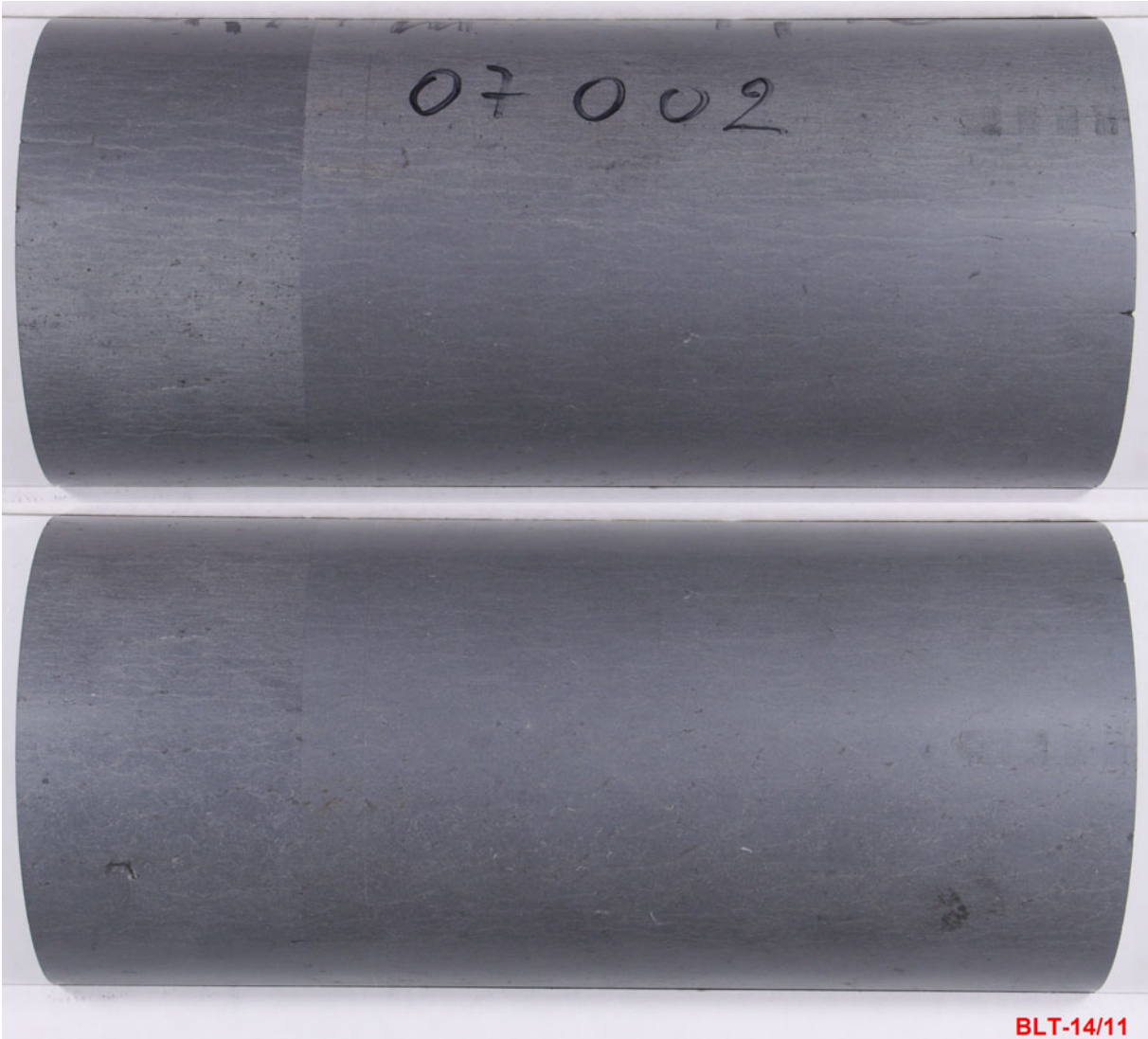
BLT-14/05

Fig. 5   The p-geometry samples BLT-14/05 and BLT-14/11 before the creep test.

BLT-15/04

Fig. 6   The s-geometry samples BLT-15/04 and BLT-15/08 before the creep test.

At both ends a disk of sintered metal was placed between the sample and the pressure plate. This provides an additional pore volume to absorb water that might leak from the sample, thus avoiding a persistent build up of pore pressure. Due to the pronounced anisotropy of hydraulic conductivity in a laminated material like Opalinus clay, this should work well for p-samples, whereas in case of s-samples, a pore pressure induced by loading the sample might persist quite a while until it dies down as a consequence of hydraulic flow.

All tests were performed under a constant cell pressure $\sigma_x = 1$ MPa. After 17 days of compaction at an axial load of $\sigma_z = 2$ MPa, creep was investigated in a multi-step loading scheme applying axial stresses of 6, 9, 11 and 14 MPa. (Note the sign convention used throughout this report: Compressive stresses and strains are defined as positive, extensive stresses and strains as negative.) Each level lasted at least 30 days. According to sample availability the tests on BLT-15 samples were started three month later than those from BLT-14.

4.2 RESULTS

The observed deformations of the four samples are shown in Fig. 7. Overall, the deformations are very small and none of the samples exhibits a significantly increasing deformation for deviatoric stresses $\sigma_{dev} = \sigma_1 - \sigma_3$ up to 10 MPa (**Fehler! Verweisquelle konnte nicht gefunden werden.**). Thus, no creep

could be found in these tests for $\sigma_{dev} \leq 10$ MPa. Surprisingly, indications of an increase in sample length are found in several cases (yellow shading in **Fehler! Verweisquelle konnte nicht gefunden werden.**), two of them even showing correlations with $R^2 > 0.6$ (BLT-15/04 at $\sigma_{dev} = 5$ MPa, BLT-14/05 at $\sigma_{dev} = 8$ MPa). There is no temperature drift that might explain these paradoxial observation. Therefore, it is most likely attributable to some drift of the displacement measurement system.

There are indications of creep in three of the four samples for a deviatoric stress of $\sigma_{dev} = 13$ MPa (**Fehler! Verweisquelle konnte nicht gefunden werden.**, Fig. 8). But these deformations still do not exceed the preceeding fluctuations significantly. In particular, the observed rates of deformation are of the same order as the largest "paradoxical extension rates" mentioned above. Thus, the calculated creep rates $d\varepsilon/dt$ include a high level of uncertainty. Nevertheless, the $d\varepsilon/dt$-values are clearly below the values reported from various studies (compiled in CZAIKOVSKI ET AL., 2006, fig.4.31). Further investigations are required to decide whether this is caused by the drained test condition.

Overall, the result is in good agreement with the fact, that a pronounced anisotropy of the in-situ stress field is found in the Opalinus clay at Mont Terri with maximum deviatoric stresses between 3 and 7 MPa (reported by several investigators, summarized in HEITZMANN & TRIPET, 2003). Any material which is able to creep tends to release shear stresses and to approach a hydrostatic state. Therefore, no creep had to be expected at least up to the mentioned level of deviatoric stress.

Tab. 2 Results from the drained creep tests. The slopes $d\varepsilon/dt$ are calculated by linear regression. For the sake of clarity, results with very poor correlations ($|R| < 0.6$) are printed grey. Yellow shading indicates phases with increasing sample length. For $\sigma_{dev} = 13$ MPa there are indications of creep in all samples except BLT-14/11.

	sample	BLT-14/05	BLT-14/11	BLT-15/04	BLT-15/08
$\sigma_{dev} = 5$ MPa	$d\varepsilon/dt$ [1/d]	$-8.8 \cdot 10^{-8}$	$-3.0 \cdot 10^{-7}$	$-7.2 \cdot 10^{-7}$	$-2.7 \cdot 10^{-8}$
	R^2	0.08	0.20	0.63	0.01
	RMSE	$3.1 \cdot 10^{-6}$	$6.3 \cdot 10^{-6}$	$6.2 \cdot 10^{-6}$	$2.6 \cdot 10^{-6}$
$\sigma_{dev} = 8$ MPa	$d\varepsilon/dt$ [1/d]	$-6.2 \cdot 10^{-7}$	$9.3 \cdot 10^{-8}$		
	R^2	0.79	0.03		
	RMSE	$5.0 \cdot 10^{-6}$	$9.1 \cdot 10^{-6}$		
$\sigma_{dev} = 10$ MPa	$d\varepsilon/dt$ [1/d]	$-8.0 \cdot 10^{-8}$	$-2.0 \cdot 10^{-7}$	$1.4 \cdot 10^{-7}$	$2.1 \cdot 10^{-7}$
	R^2	0.07	0.10	0.09	0.35
	RMSE	$6.6 \cdot 10^{-6}$	$1.4 \cdot 10^{-5}$	$7.0 \cdot 10^{-6}$	$4.3 \cdot 10^{-6}$
$\sigma_{dev} = 13$ MPa	$d\varepsilon/dt$ [1/d]	$3.75 \cdot 10^{-7}$	$-1.4 \cdot 10^{-7}$	$4.3 \cdot 10^{-7}$	$1.5 \cdot 10^{-7}$
	R^2	0.74	0.09	0.61	0.40
	RMSE	$4.6 \cdot 10^{-6}$	$9.6 \cdot 10^{-6}$	$7.1 \cdot 10^{-6}$	$3.8 \cdot 10^{-6}$
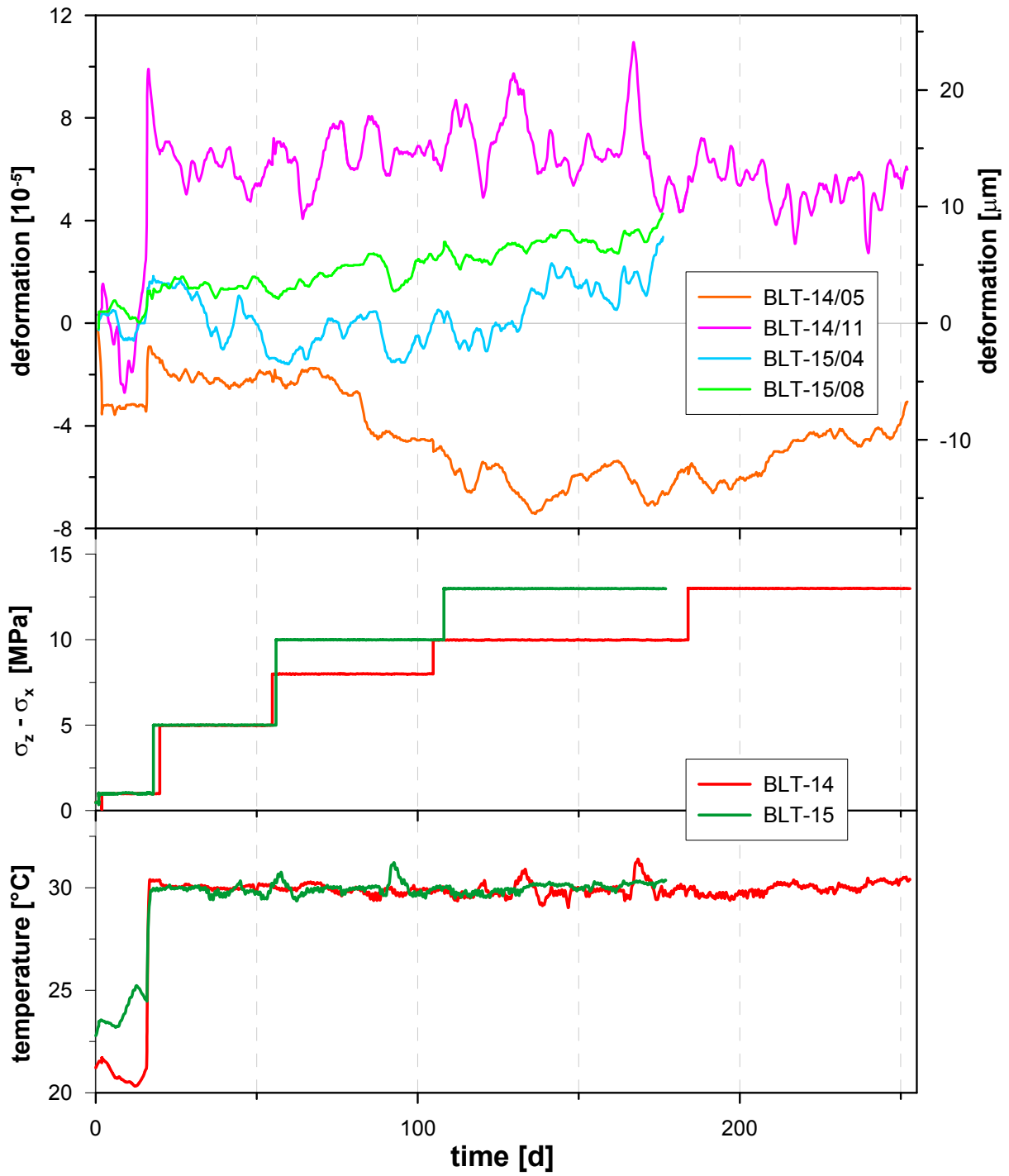
Fig. 7 Results from the drained creep tests. The deformations are displayed as running averages over 21 data points.
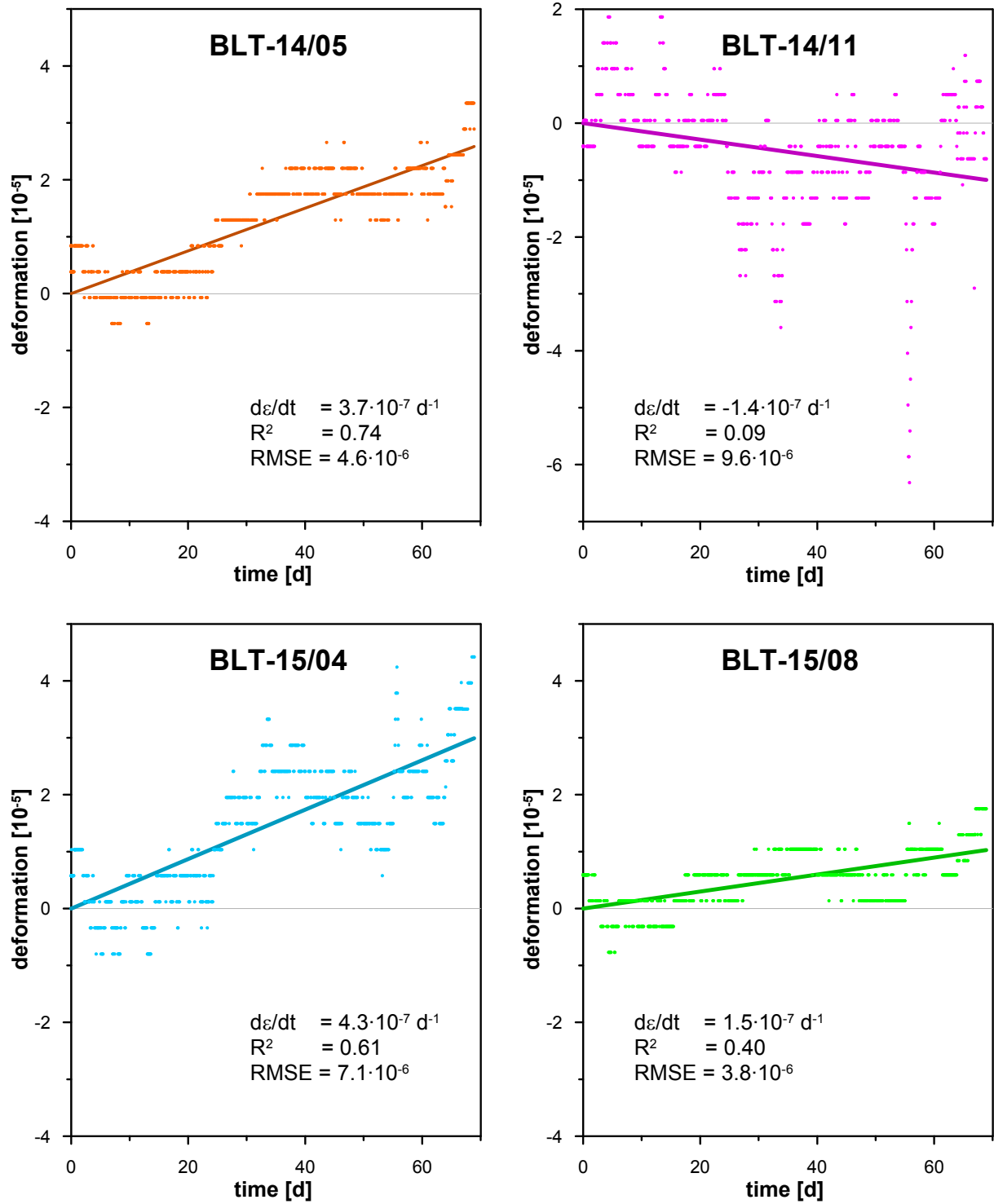
Fig. 8 The creep behavior of the four samples during the test phase with $\sigma_{dev} = 13$ MPa. Data and linear regression lines are shown. Deformations are given relative to the "calculated initial state" of this phase (taken from the linear fit). The alignment of the measured data in horizontal lines displays the impact of the resolution δl_{meas} of the combination of A/D-converter and displacement transducer. $\delta l_{meas} = 10^{-6}$ m. corresponds to a deformation resolution of $\delta \varepsilon_{meas} = 4.6 \cdot 10^{-6}$.

5 COMPLEX STRENGTH TEST

5.1 CONCEPT AND OBJECTIVE

It was the idea of this test to gain as much information as possible about elastic parameters, the onset of damage (irreversible deformation, dilatancy etc.), the shear strength, and the residual strength from a single sample. Furthermore, possible pore pressure effects upon these quantities should be investigated. A Karman cell equipped with a very versatile control and data acquisition system was chosen for this purpose. It allows for the execution of virtually any type of stress-strain-path.

A test concept comprising three sections was developed. Section A is focused on the investigation of the onset of damage, section B deals with shear strength, and section C analyses residual strength. In any section investigations are to be done at various minimum principle stresses (i.e. confining pressures).

All loading phases of the complex strength test were carried out under deformation control at a rate of $d\varepsilon_1/dt = 10^{-7}\,s^{-1}$. Hydrostatic compaction at 5 MPa over 3 days preceded the first test section. This roughly corresponds to the in situ mean normal stress at the Mont Terri test site.

Strictly undrained conditions are required during the test because the detection of possible pore pressure effects on the investigated material properties are another objective.

5.1.1 Test section A – limit of linear elasticity

Obviously, the onset of damage must be detected very carefully, if it should be investigated repeatedly at several levels of confining pressure. To avoid damaging the sample too much, thus changing its properties significantly and impeding further investigations of an "undisturbed sample", a rather strict and well detectable criterion for the beginning damage is required. Since all sample deformations are fully reversible within the range of linear elastic behavior, the limit of linear elasticity might be the very first evidence for incipient damage. Although it is possibly far below any level of relevant material damage (such as measurable dilatancy or even failure), it nevertheless characterizes the transition to another deformation regime, either to a non-linear elastic behavior or to an irreversible alteration of material properties.

To investigate the limit of linear elasticity test section A consists of a sequence of loading cycles. Each cycle comprises three phases as illustrated in Fig. 9. First, the sample is loaded with a constant rate of deformation. As soon as a deviation of the axial stress from a linear path can be detected the loading is stopped. The sample is unloaded at a rate of $d\sigma_1/dt = -0.1$ MPa/min. In the third phase the confining pressure is increased while keeping the axial stress constant.

The main challenge of this concept is the reliable and "near real time" detection of the deviation from linear elasticity. There are several instances that make this task difficult:
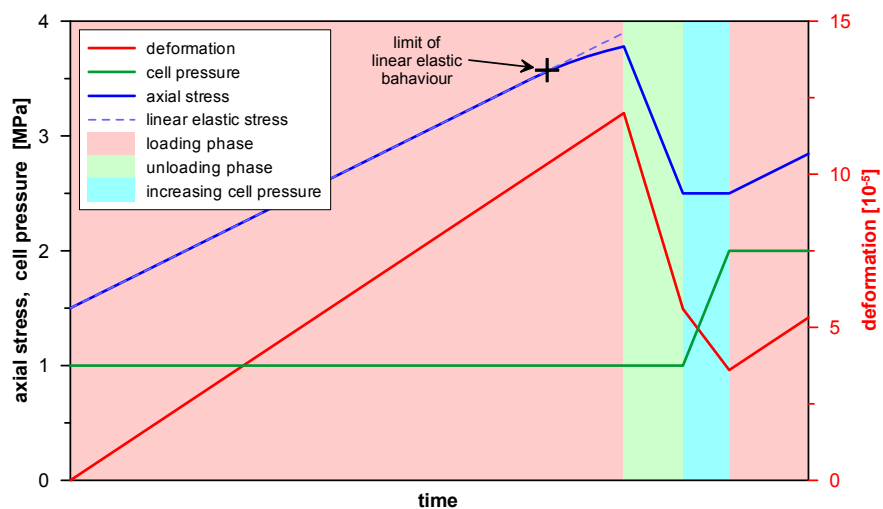
Fig. 9 Sketch of loading cycles performed in section A of the complex strength test.

– The slope of the deviatoric stress vs. deformation relationship will usually depart from the constant Young's modulus continuously, thus to some extent making the determination of the linear elastic limit a question of measuring accuracy.

– Due to measurement noise, observations will always fluctuate a bit around an idealized linear relationship (Fig. 10). This blurs the onset of a systematic deviation from linear elasticity and particularly hampers the development of an algorithm for automatic detection.

– Any disturbance of the process control or data acquisition can interfere with the detection of the linear elastic limit. As shown in Fig. 10, abrupt drops ("spikes") in deviatoric stress (-0.5 to -1.5 MPa, typically lasting 2 minutes) accidentally occurred in the measurements. They are most likely a result of a minute tilting of the load piston. They obviously do not affect the sample behavior, but sometimes disturb the determination of the linear elastic limit. Spikes were eliminated from the data by an appropriate filter.
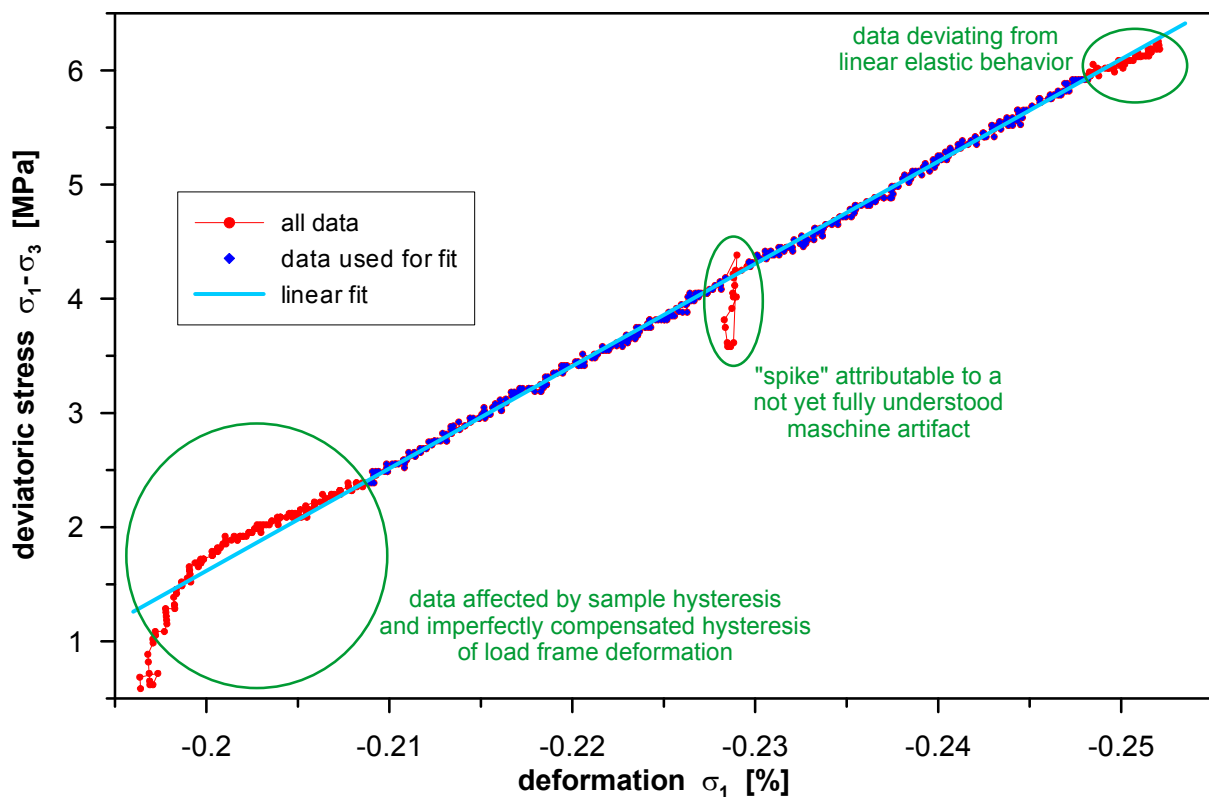
Fig. 10 Example of a loading phase performed on a BHE-B1 sample to determine the linear elastic limit. The confining pressure during this loading was $\sigma_3 = 19\,MPa$.

– Hysteresis effects of the sample interfere with the linear elastic behavior. They usually lead to an initial slope of the deviatoric stress vs. deformation relationship which is much steeper than the Young's modulus. The curve will then bend asymptotically towards the linear relationship. Sometimes, this makes it difficult to determine a linear part of the curve unambiguously and may also lead to an overestimation of the Young's modulus. In extreme cases, the hysteresis effects might not fade sufficiently until the linear elastic limit is reached.

– The loading frame of any triaxial apparatus will exhibit an elastic deformation depending on the axial load. This frame deformation has to be considered as a correction term in the acquisition of deformation data. In case of the used triaxial apparatus which is designed for axial forces up to 2500 kN the deformation characteristic is distinctly non-linear (Fig. 11). This is particularly true in the lower load range up to 500 kN which is applied in the investigation of Mont Terri Opalinus clay

material. Any error in the quanti-
fication of the frame deforma-
tion will result in a non-linear er-
ror of the calculated sample de-
formation and might conceal
linearity.

A small but distinct hysteresis of
the frame deformation (Fig. 11)
even aggravates this problem.
Currently, there is no satisfac-
tory correction available for this
effect. Therefore, an extensive
routine of calibration measure-
ments is on the way to gain an
improved description of the
frame deformation for use in fu-
ture experiments as well as for
reprocessing of the existing data sets.
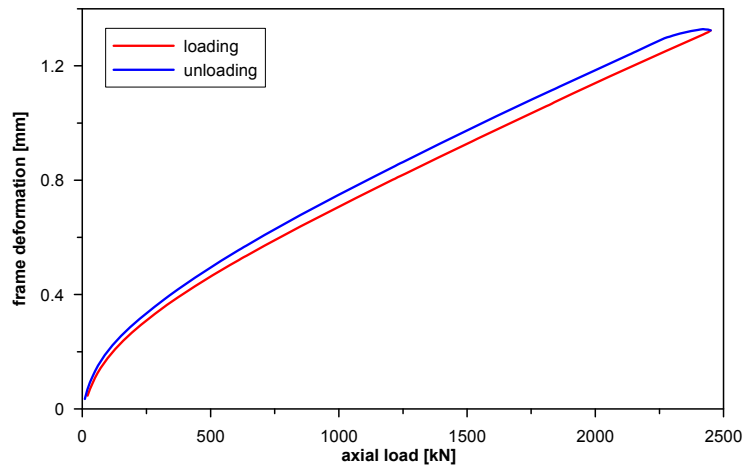
Fig. 11 The loading frame deformation of the used triaxial apparatus exhibits a strong non-linearity as well as a distinct hysteresis.

Actually it seems to be too difficult to develop an algorithm for an automatic determination of the linear elastic limit. Consequently, tools are required to aid the operator to recognize in sufficient time when the loading has exceeded the linear elastic limit. Obviously, it is not possible to accomplish this task by means of a simple deviatoric stress vs. deformation plot (Fig. 10).

A self-evident approach is to use a $d\sigma_1/d\varepsilon_1$-plot. Unfortunately, even a moderate noise in a data set can disturb the calculation of a derivative dramatically (see Fig. 12 for the impact of noise and smoothing on the $d\sigma_{dev}/d\varepsilon_1$-curve). The calculation of the derivative has to be based on a data set the range of which ("smoothing window") is significantly bigger than the noise (in both variables!) to overcome this problem. In return the smoothing effect of a bigger window leads to increasing errors of the calculated derivative in regions where the $d\sigma_1/d\varepsilon_1$-curve bends – which is particularly the case at the linear elastic limit. Furthermore, a broad smoothing will result in a tendency to localize the beginning of a bending too early (Fig. 12). Finally, a broad smoothing also hampers the goal of near real time detection of the linear elastic limit since it delays the data availability by a half width of the smoothing window. Altogether, the $d\sigma_{dev}/d\varepsilon_1$-curve is not a perfect tool for a timely detection of the linear elastic limit. Nevertheless, it turned out to be helpful in some cases, especially when several variably smoothed $d\sigma_{dev}/d\varepsilon_1$-curves are plotted simultaneously.

A "reduced stress" plot, i.e. a plot of the deviation of axial stress from a pure linear elastic behavior ($\sigma_{red}(\varepsilon_1) = \sigma_1(\varepsilon_1) - \sigma_{lin}(\varepsilon_1)$), turned out to be the most efficient tool for the detection of the linear elastic limit. As for the $d\sigma_{dev}/d\varepsilon_1$-plot, smoothing (by running average) is required in case of noisy data. But a smaller smoothing window is sufficient because there is no calculation of differential quantities required. Fig. 13 shows the $\sigma_{red}(\varepsilon_1)$-plot for the same artificial data set used in Fig. 12. Note that the largest smoothing window used in Fig. 13 and the smallest used in Fig. 12 are identical. Contrary to $d\sigma_{dev}/d\varepsilon_1$-plots, there is a slight tendency to localize the linear elastic limit too late when using $\sigma_{red}(\varepsilon_1)$-plots.

The application of the $d\sigma_{dev}/d\varepsilon_1$-plot as well as the $\sigma_{red}(\varepsilon_1)$-plot on the measured data set of Fig. 10 is displayed in Fig. 14.
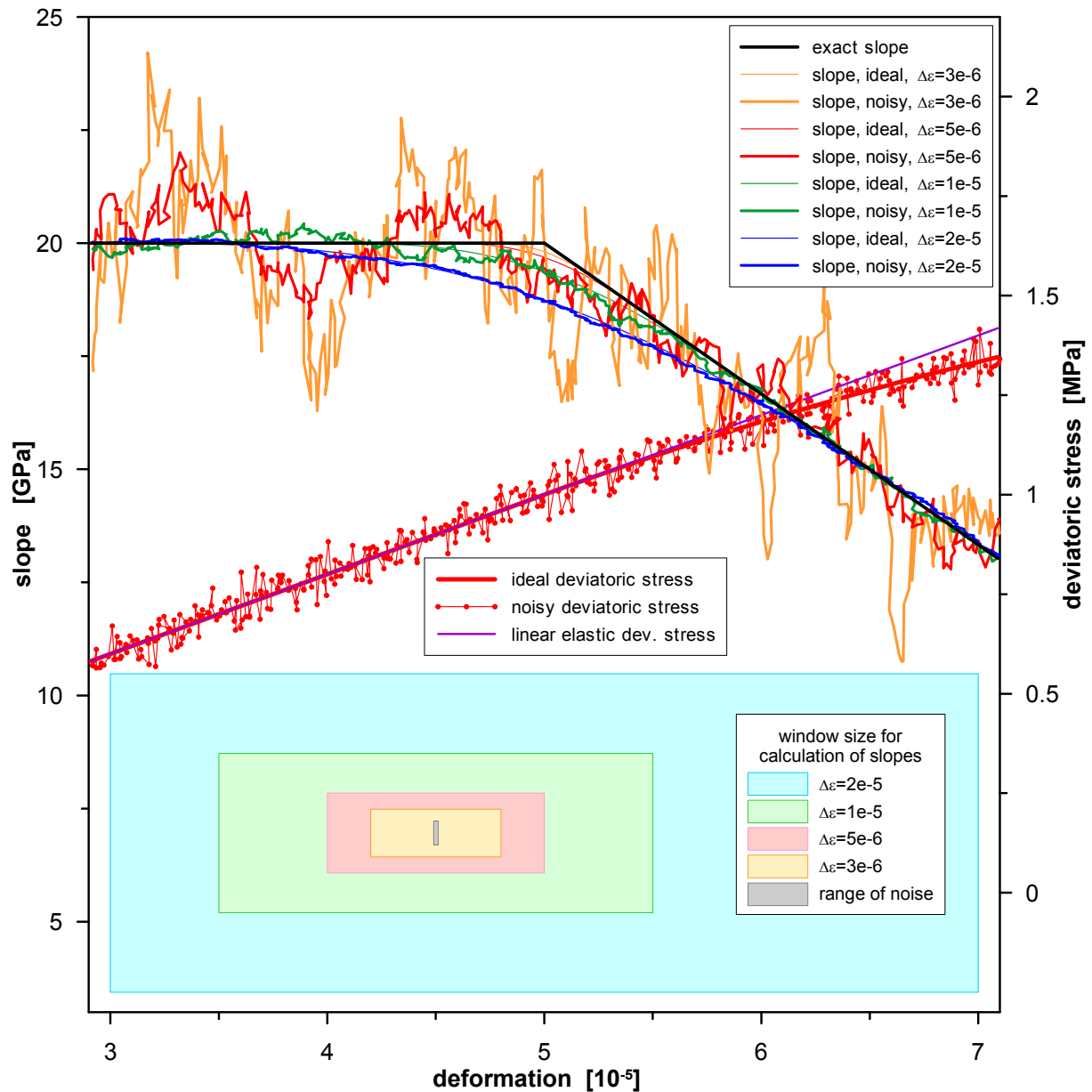
Fig. 12 The impact of data noise and smoothing on a calculated $d\sigma/d\varepsilon$-curve shown by a synthetic data set. The assumed material behavior is given by $E = 20\,GPa$, a linear elastic limit of $\varepsilon_{lin} = 5 \cdot 10^{-5}$, and a decreasing stiffness $d\sigma/d\varepsilon = (1 - (\varepsilon - \varepsilon_{lin})/6 \cdot 10^{-5})\,E$ for $\varepsilon_{lin} < \varepsilon < 11 \cdot 10^{-5}$. Besides the "ideal" (noiseless) data, a noisy data set is presented. A normal distributed noise with standard deviations $\delta\varepsilon = 10^{-7}$ and $\delta\sigma = 0.03\,MPa$ was added to the ideal data. A sampling rate of one measurement per deformation increment of 10^{-7} is assumed.

Slopes $d\sigma/d\varepsilon$ were calculated by linear regression analysis from the data within a smoothing window with a half width $\Delta\varepsilon$. Slopes were calculated for various sizes of smoothing windows which are represented at the bottom of the plot including the size of the corresponding σ-window $\Delta\sigma = E\,\Delta\varepsilon$.

The dilemma between an increasing systematic deviation from the exact slope for increasing width of the smoothing window, and an increasing statistical noise for decreasing width of the smoothing window is obvious.
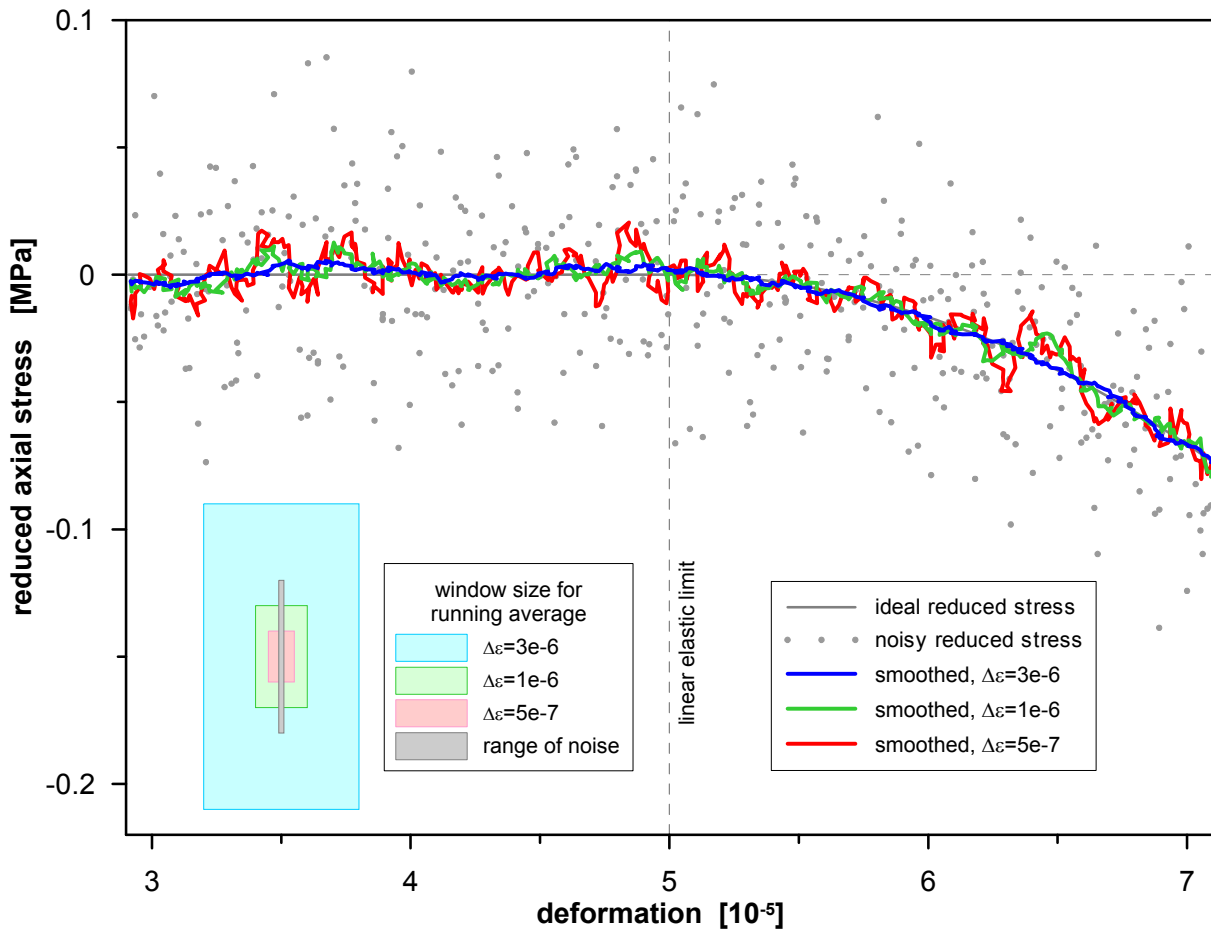
Fig. 13   For the synthetic data set used in Fig. 12 the "reduced stress" plot $\sigma_{red}(\varepsilon) = \sigma_1(\varepsilon) - \sigma_{lin}(\varepsilon)$ indicates the linear elastic limit more reliably than a $d\sigma/d\varepsilon$-plot. It is particularly less susceptible towards noisy data. The size of the smoothing windows used for the calculation of running averages is shown in the same way as in Fig. 12.
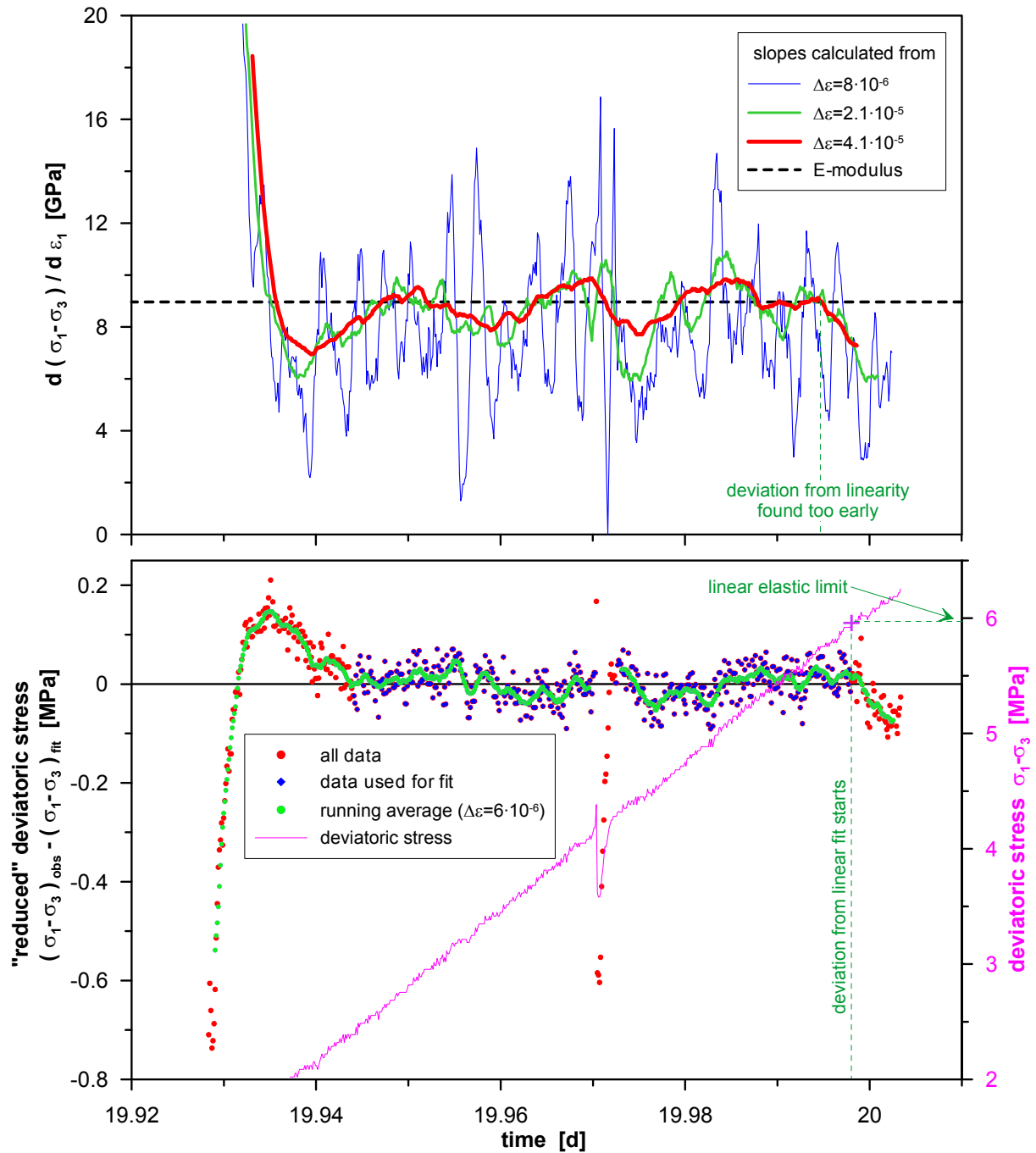
Fig. 14 The $d\sigma_{dev}/d\epsilon_1$-plot as well as the $\sigma_{red}(\epsilon_1)$-plot for a loading phase performed on a BHE-B1 sample to determine the linear elastic limit. The confining pressure during this loading was $\sigma_3 = 19$ MPa.

5.1.2 Test section B – shear strength

Overall test section B is a conventional strength test. It differs only in the attempt to measure the shear strength of a single sample repeatedly at different confining pressures σ_3. The loading of the sample was therefore stopped immediately as soon as the $\sigma_1(\varepsilon)$-curve became horizontal. Nevertheless, the problem already mentioned in chapter 5.1.1 arises by far more severe in this test section: The onset of any type of damage can only be tested once on an "undisturbed sample". It must be expected that only very few measured peak stresses approximately represent properties of the undamaged material. After a few loading cycles, the progressive damage of the sample will change its properties gradually towards the residual properties.

5.1.3 Test section C – residual strength

Test section C is a conventional test of residual strength. This can be repeated for various levels of confining pressure σ_3. No particular problems have to be expected as long as the required deformation does not become too large and the sample integrity is not destroyed.

5.2 RESULTS

There was no experience with the execution of a triaxial test as complex as the one outlined before. Particularly the tools and techniques required for timely decisions concerning the termination of loading phases could not be validated before. Hence, a serious risk to significantly damage the sample ahead of schedule was suspected. At that time there were only rather few well preserved samples available from the boreholes BLT-14 to BLT-16. Therefore, a "less valuable" sample from borehole BHE-B1 was chosen for the "risky" first test. The sample was in p-geometry. Its diameter was 100 mm, the length 200 mm. Although stored in a sealed plastic bag (but not in the new liners shown in Fig. 3) since 2002, it displays some clear indications of damage by drying such as shrinkage cracks (Fig. 15). This of course reduces the chance to find any pore pressure effects during the experiment.

The full test program could be carried out within 53 days without relevant problems. During section A a leakage in the hydraulic system controlling the axial load resulted in an automatic shutdown of the triaxial apparatus. But since the sample was not damaged the experiment could be continued.

The confining pressure was increased from 1 MPa up to 21 MPa in steps of 1 MPa in section A and B. Some pressure steps were skipped in section C. Otherwise, the very long loading phases required to reach the residual strength might have resulted in too large sample deformations that can destroy sample integrity or damage some sensors located inside the triaxial cell. The complete stress path of the experiment is shown in Fig. 16. The occurrence of spikes (see chapter 5.1.1) is quite conspicuous in these plots. However, they did not harm the sample and did not affect the experimental results except for a few cases where a spike occurs very close to the linear elastic limit and interferes with its detection.

BHE-B1/001/15

Fig. 15   The BHE-B1/001/15 sample used in the complex strength test. Some shrinkage cracks parallel to the bedding indicate desiccation of the material.
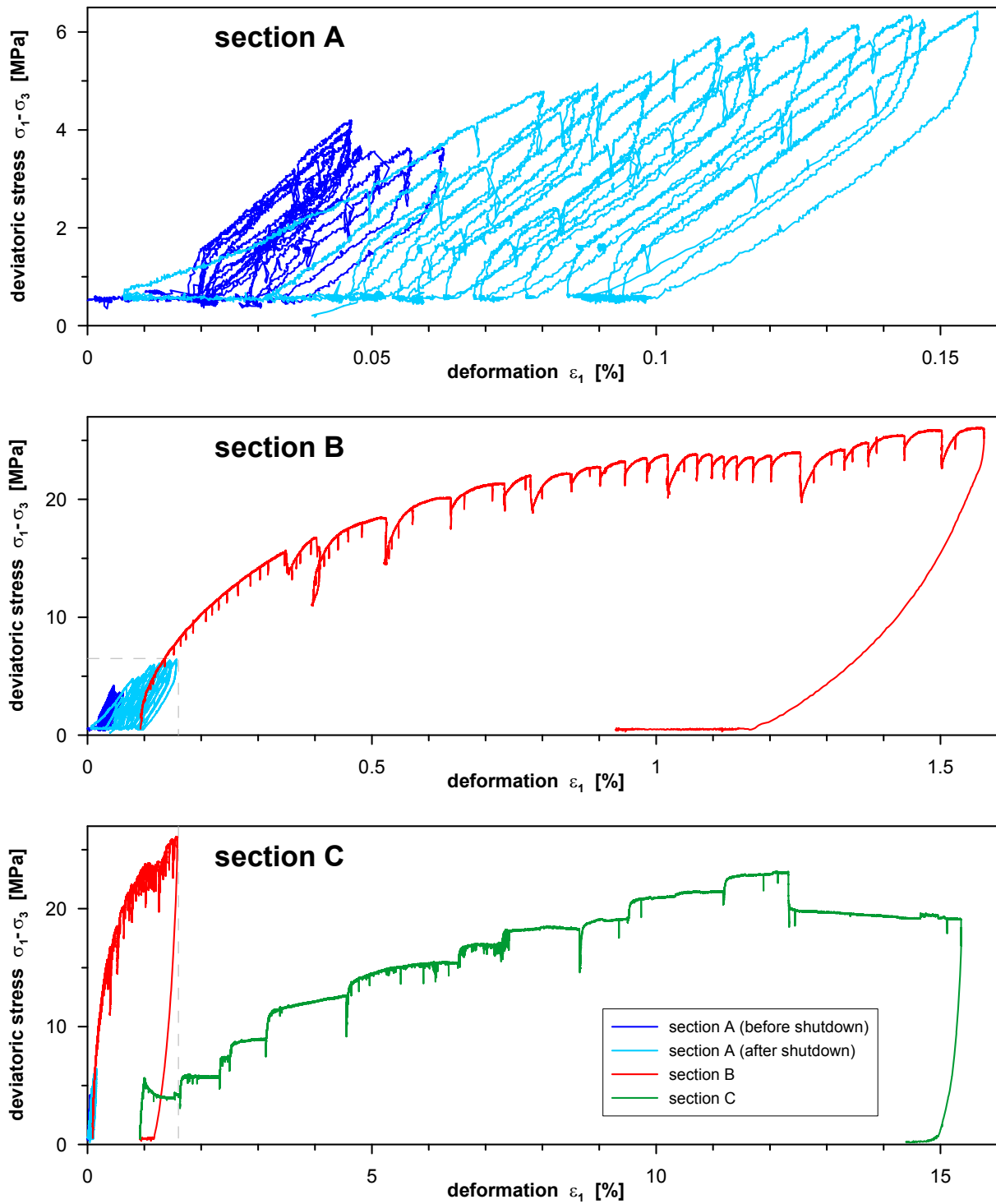
Fig. 16   The stress-deformation-path $\sigma_{dev}(\varepsilon_1)$ during the three test sections. In plot B and C the area of the previous plot is indicated by a grey dashed line.

5.2.1 Test section A – limit of linear elasticity

The linear elastic limit was found to exhibit a linear dependency from the minimum principle stress σ_3 (Fig. 17, Tab. 3):

$$\sigma_{lin} = (\sigma_1 - \sigma_3)_{lin} = a_0 + a_1\,\sigma_3 \qquad \text{where} \quad a_0 = 2.60\ \text{MPa} \quad \text{and} \quad a_1 = 0.1615$$

These values are surprisingly small – for instance, they are less than 1/6 of the shear strength (see below). The linear elastic limit will therefore fall clearly below common damage criteria as the dilatancy limit.

Concerning the effectiveness of the tools used to determine the linear elastic limit a satisfactory (but not a perfect) success was found. In some cases there is still an element of subjectiveness in the selection of the data range used to define the linear elastic curve.
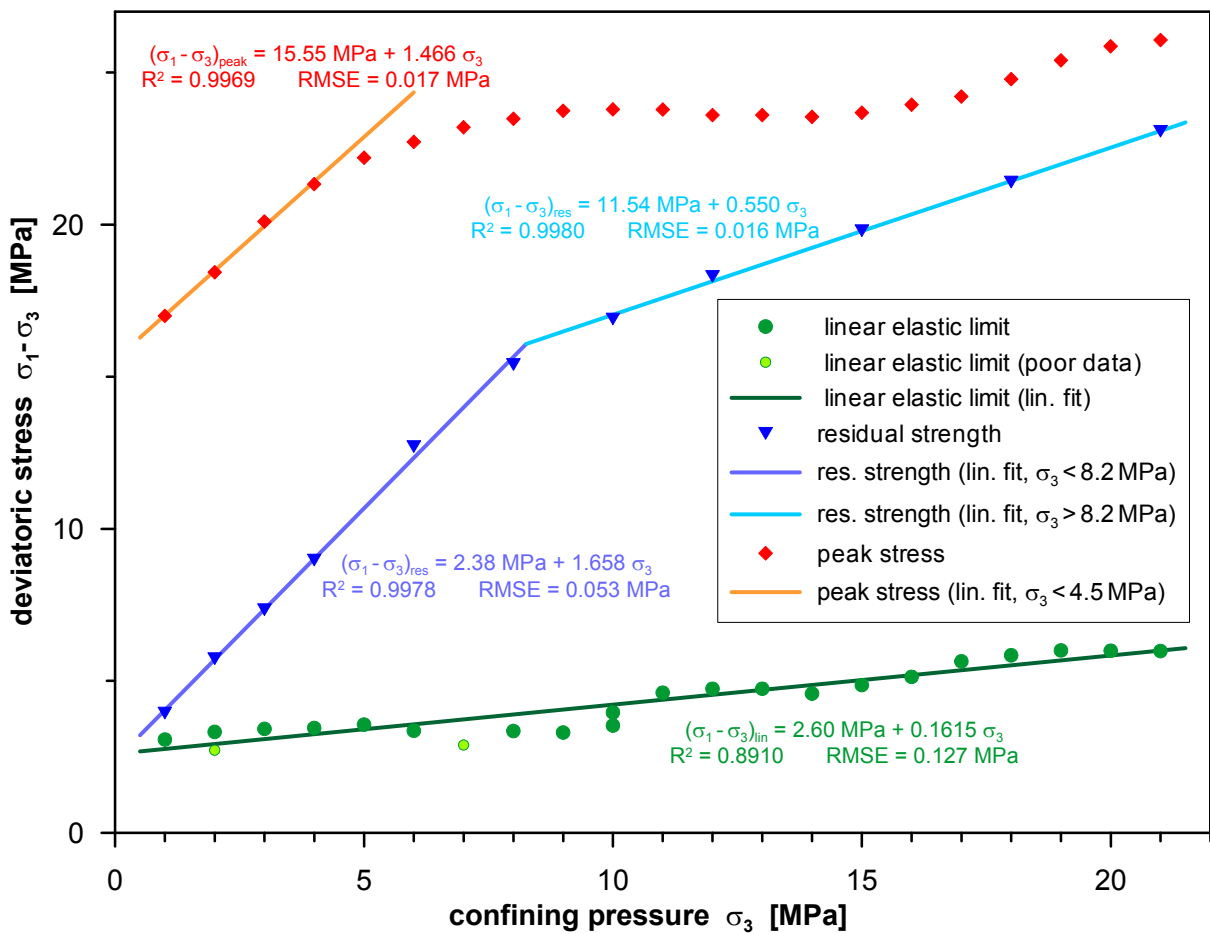
Fig. 17   Linear elastic limit, peak stress and residual strength measured on a single BHE-B1 sample in the complex strength test.

Tab. 3 Fitted $\sigma_{dev}(\sigma_3)$-relationships for the linear elastic limit, peak stress (shear strength) and residual strength measured on a single BHE-B1 sample in the complex strength test.

	basis of fit			R^2	RMSE [MPa]	fit $\sigma_{dev} = a_0 + a_1\sigma_3$	
	$\min(\sigma_3)$ [MPa]	$\max(\sigma_3)$ [MPa]	n			a_0 [MPa]	a_1
linear elastic limit	1	21	21	0.8910	0.127	2.60	0.1615
shear strength	1	4	4	0.9969	0.017	15.55	1.466
residual strength	1	8	6	0.9978	0.053	2.38	1.658
residual strength	9	21	5	0.9980	0.016	11.54	0.550

As the $\sigma_{lin}(\sigma_3)$-relationship is linear throughout the investigated range, there is no indication of any pore pressure effect. To understand how pore pressure effects should appear, a brief description of the theory might be useful:

According to Terzaghi's effective stress theory (TERZAGHI, 1936), the effective stress[1] tensor $\underline{\sigma}'$ governs the deformation and damage of a material, and it is given by $\underline{\sigma}' = \underline{\sigma} - u \cdot \underline{1}$ (where $\underline{\sigma}$ is the total stress tensor, u is the pore pressure, and $\underline{1}$ denotes the unity tensor). Consequently, a pore pressure does not affect shear stresses but reduces normal stresses. Any constitutive equations as well as stability criteria (e.g. the Mohr-Coulomb relationship) have to be written in effective stresses instead of total stresses.

Thus, a linear stability criterion like $\sigma_{lin} = (\sigma'_1 - \sigma'_3)_{lin} = a_0 + a_1\sigma'_3$ is equivalent to $\sigma_{lin} = (\sigma_1 - \sigma_3)_{lin} = a_0 + a_1(\sigma_3 - u)$. In case that a pore pressure develops due to compaction when σ'_3 or $\sigma'_{oct} = (\sigma'_1 + \sigma'_2 + \sigma'_3)/3$ exceeds a certain limit, the $\sigma_{lin}(\sigma_3)$-curve will be linear only up to the point where pore pressure starts to develop, and will fall below the linearity beyond this point. This would be a typical appearance of pore pressure effects.

It should be mentioned that there are more elaborate theories of hydro-mechanic coupling (e.g. SKEMPTON, 1960). But even for those theories that use fundamentally different concepts than Terzaghi's approach (e.g. FREDLUND & MORGENSTERN, 1977), the predicted pore pressure effects are essentially similar.

Besides the determination of the linear elastic limit, Young's modulus E in axial direction (i.e. parallel to the foliation of the Opalinus clay) could be calculated from section A data (Fig. 18). Results from loading and unloading phases were in good agreement. For $\sigma_3 > 5.5$ MPa a constant value $E = 8.61 \pm 0.13$ GPa was found. The increased and very scattered results for $\sigma_3 < 5.5$ MPa might be an artifact arising from deficiencies in the compensation of load frame deformation. This question will not be resolved until the new calibration data will be available.

---

[1] The term "effective stress" in this context must not be confused with the elsewhere used "effective shear stress" $\tau_{eff} = \sqrt{(\sigma_1 - \sigma_{oct})^2 + (\sigma_2 - \sigma_{oct})^2 + (\sigma_3 - \sigma_{oct})^2}$
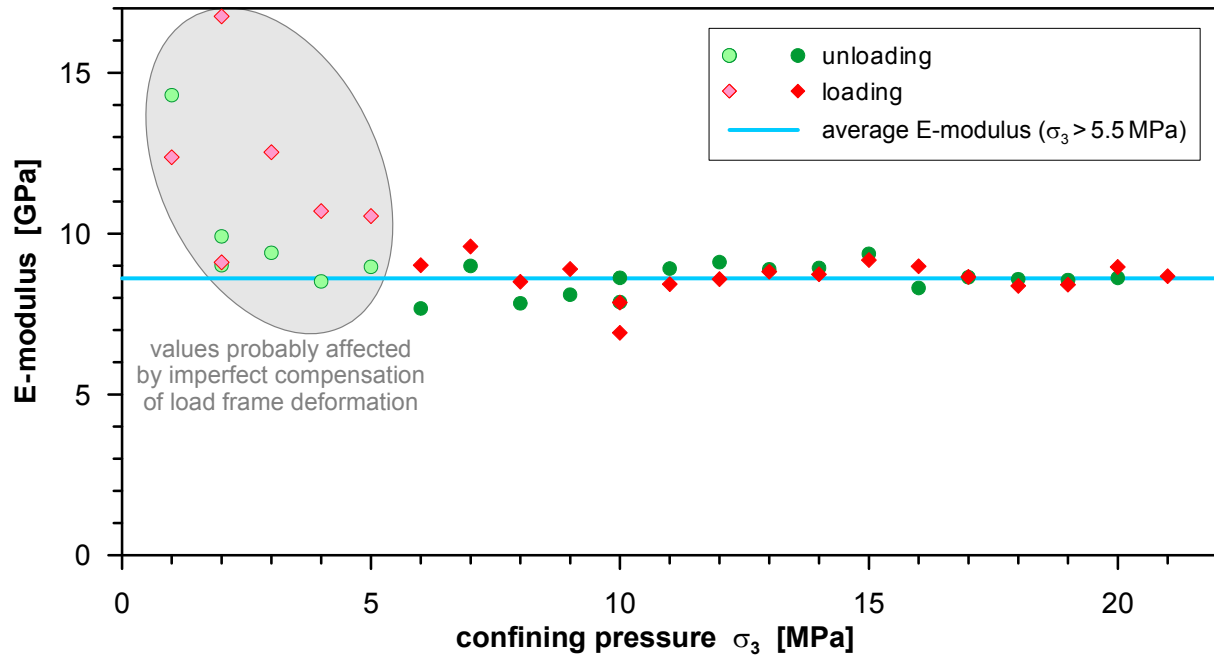
Fig. 18   Observed Young's modulus of a BHE-B1 sample in the complex strength test.

5.2.2 Test section B – shear strength

The observed peak stresses $\sigma_{peak} = (\sigma_1 - \sigma_3)_{peak}$ show a linear increase up to a confining pressure of approx. 4 MPa (Fig. 17). Thereafter the $\sigma_{peak}(\sigma_3)$-curve gradually flattens to a plateau and even to a slight decrease, until it starts to increase again for $\sigma_3 > 15$ MPa. The initial linear part is described by (Tab. 3):

$$\sigma_{peak} = a_0 + a_1\,\sigma_3 \qquad\qquad \text{where} \quad a_0 = 15.55\,\text{MPa} \quad \text{and} \quad a_1 = 1.466$$

Assuming an isotropic material (which of cause is not the case for the Mont Terri Opalinus clay) this would correspond to a Mohr-Coulomb line with a cohesive shear $k = 4.95$ MPa and a friction angle $\varphi = 25.0°$. Then the normal vector to the plane of shear failure should form an angle of $\beta = 45° + \varphi/2 = 57.5°$ relative to the direction of the largest principle stress (i.e. the axis of the sample). Actually, $\beta = 68°$ was found for the sample (Fig. 19). This discrepancy clearly points out the anisotropic nature of the Opalinus clay and corresponds to the expected rotation of the shear plane towards the bedding plane.

The flattening of the $\sigma_{peak}(\sigma_3)$-curve beyond $\sigma_3 = 4$ MPa is most likely attributable to a progressive damage of the sample during test section B. While a distinct shear plane was formed, the properties of the sample gradually approached the residual state and its strength falls far below the original shear strength. This hypothesis is also strengthened by the observation that the slope of the terminal increase of the $\sigma_{peak}(\sigma_3)$-curve is close to the slope of the residual strength found in section C.

The observed $\sigma_{peak}(\sigma_3)$-curve can hardly be explained by pore pressure effects. Whereas the flattening of the curve would agree with pore pressure effects, the slight decrease around $\sigma_3 = 13$ MPa and the subsequent increase does not correspond with theoretical postulations. Nevertheless, there is no basis for a definite decision concerning the occurrence of pore pressure effects during section B, as they might be concealed by the impact of progressive sample damage.

BHE-B1/001/15

Fig. 19 The BHE-B1/001/15 sample after the complex strength test. Although the shear failure condition was reached for the first time at an axial deformation $\varepsilon_1 = 0.0046$, the test was continued up to $\varepsilon_1 = 0.155$ during section C. This resulted in the formation of very distinctive primary and secondary shearing interfaces. The shear planes are inclined by approx. 22° versus the sample axis.

5.2.3 Test section C – residual strength

The behavior of the sample during section C was rather heterogeneous with respect to the shape of the $\sigma_{dev}(\varepsilon)$-curves for different confining pressures and the deformations required to reach a constant residual stress state (Fig. 16). Regardless this somewhat erratic behavior the observed residual strength values $\sigma_{res} = (\sigma_1 - \sigma_3)_{res}$ display a very clear picture. The $\sigma_{res}(\sigma_3)$-curve consists of two linear braches (Fig. 17, Tab. 3):

$$\sigma_{res} = a_0 + a_1\sigma_3 \qquad \text{where} \quad a_0 = 2.38\,\text{MPa} \quad \text{and} \quad a_1 = 1.658 \quad \text{for} \quad \sigma_3 < 8.26\,\text{MPa}$$
$$a_0 = 11.54\,\text{MPa} \quad \text{and} \quad a_1 = 0.550 \quad \text{for} \quad \sigma_3 > 8.26\,\text{MPa}$$

The buildup of pore pressure for minimum principle stresses $\sigma_3 > 8$ MPa is a possible explanation of this curve. However, without pore pressure measurements during the test, there is no positive affirmation of this interpretation.

6 SUMMARY AND PERSPECTIVE

DRAINED CREEP TEST:

- In drained creep tests no creep could be detected for a deviatoric stress $\sigma_{dev} \leq 10\,\text{MPa}$. At $\sigma_{dev} = 13\,\text{MPa}$ indications of creep were found but require further validation. The observed creep rates $d\varepsilon/dt \approx 4 \cdot 10^{-7}\,\text{d}^{-1}$ are clearly below other published creep test results from Mont Terri Opalinus clay.

- More creep tests including longer observation time are required to validate the low creep rates.

- Actually, the samples are still loaded with $\sigma_{dev} = 13\,\text{MPa}$ at an increased temperature of 50°C to investigate the influence of temperature. Undrained tests on the samples after saturation are planned to assess the impact of pore pressure.

COMPLEX STRENGTH TEST:

- The tested experimental approach turned out to be suitable to determine the linear elastic limit as well as the residual strength over a wide range of confining pressure on a single sample. A sample in p-geometry was tested.

- The linear elastic limit can be described by $\sigma_{lin} = (\sigma_1 - \sigma_3)_{lin} = 2.60\,\text{MPa} + 0.1615\,\sigma_3$. Young's modulus is determined as $E = 8.61 \pm 0.13\,\text{GPa}$.

- The residual strength shows two linear branches which might indicate a pore pressure effect:
$$\sigma_{res} = 2.38\,\text{MPa} + 1.658\,\sigma_3 \quad \text{for} \ \ \sigma_3 < 8.26\,\text{MPa}$$
$$\sigma_{res} = 11.54\,\text{MPa} + 0.550\,\sigma_3 \quad \text{for} \ \ \sigma_3 > 8.26\,\text{MPa}$$

- Due to progressive damage of the sample, peak strength can be determined for only 3 or 4 values of confining pressure. A linear relationship is found: $\sigma_{peak} = 15.55\,\text{MPa} + 1.466\,\sigma_3$.

- The complex strength test will be executed on a number of p- and s-samples. Further enhancement of the test design is intended (wider range of confining pressure, volume measurement, damage detection by ultrasonic measurements).

- For the used triaxial apparatus hysteresis of the load frame deformation turned out to be a major drawback of deformation measurement. Extensive calibration measurements and the development of a suitable hysteresis model will be carried out to overcome this problem.

7 REFERENCES

CZAIKOVSKI, O., WOLTERS, R., DÜSTERLOH, U. AND LUX, K.-H. (2006): Abschlussbericht zum BMWi-Forschungsvorhaben Laborative und numerische Grundlagenuntersuchungen zur Übertragbarkeit von Stoffmodellansätzen und EDV-Software für Endlager im Salzgestein auf Endlager im Tongestein. – Lehrstuhl für Deponietechnik und Geomechanik, Technische Universität Clausthal, Germany, 270 p.

FREDLUND, D.G. AND MORGENSTERN, N.R. (1977): Stress state variables for unsaturated soils. – ASCE J. Geotech. Eng. Div. GT5, 103,447-466.

HEITZMANN, P. AND TRIPET, J.-P. (2003): Mont Terri Project – Geology, Palaeohydrology and Stress Field of the Mont Terri Region. – Reports of the FOWG, Geology Series, No. 4, 92 p, Bern.

KLINKENBERG, M., KAUFHOLD, S., DOHRMANN, R. AND SIEGESMUND, S. (2007): Microstructural investigation of Opalinus Clay – Proposal of a carbonate distribution model. – Abstract, 3rd International Meeting: Clays in Natural & Engineered Barriers for Radioactive Waste Confinement, ANDRA, Lille, France, p. 345.

PEARSON, F.J., ARCOS, D., BATH, A., BOISSON, J.-Y., FERNANDEZ, A., GAEBLER, H.-E., GAUCHER, E., GAUTSCHI, A., GRIFFAULT, L., HERNAN, P. AND WABER, H.N. (2003): Geochemistry of Water in the Opalinus Clay Formation at the Mont Terri Rock Laboratory - Synthesis Report. – Geological Report No. 5. Swiss National Hydrological and Geological Survey, Ittigen-Berne, 319 p.

SCHNIER, H. (2004): Postdismantling laboratory triaxial strength tests. – Deliverable 8b, WP3/Task 32 Postdismantling rock mechanic analysis – Heater Experiment (HE). Federal Institute for Geosciences and Natural Resources (BGR), Hannover.

SKEMPTON, A.W. (1960). Effective stress in soils, concrete and rocks. – Proc. Conf. Pore Pressure and Suction in Soils, 4–16, Butterworth, London.

TERZAGHI, K. (1936): The shearing resistance of saturated soils and the angle between the planes of shear. – In: CASAGRANDE, A., RUTLEDGE, P.C. AND WATSON, J.D. (Eds.): Proc. 1st Int. Conf. Soil Mech. Found. Eng. Vol.1,54-56.

THURY, M. AND BOSSART, P. (1999): Results of hydrogeological, chemical and geotechnical experiments performed in 1996-1997. – Mont Terri Project. Rapport géologique n°23, Bern, 191 p.

8 LIST OF TABLES

9 LIST OF FIGURES